ELSEVIER

Polymer 42 (2001) 1207–1217

polymer

www.elsevier.nl/locate/polymer

Elongational flow-induced morphology change of block copolymers Part 1. A polystyrene-*block*-poly(ethylene butylene)-*block*-polystyrene-*block*-poly(ethylene butylene) tetrablock copolymer with polystyrene spherical microdomains

T. Kotaka[a,*], M. Okamoto[a], A. Kojima[a,1], Y.K. Kwon[a], S. Nojima[b]

[a]*Advanced Polymeric Materials Engineering, Graduate School of Engineering, Toyota Technological Institute, Hisakata 2-12-1, Tempaku, Nagoya 468-8511, Japan*

[b]*School of Materials Science, Japan Advanced Institute of Science and Technology (JAIST), Tatsunokuchi, Ishikawa 923-12, Japan*

Received 3 February 2000; received in revised form 29 May 2000; accepted 5 June 2000

Abstract

Simultaneous measurements of transient tensile stress and birefringence are conducted as a function of Hencky strain rate $\dot{\epsilon}_0$ and elongation time t on a polystyrene-*block*-poly(ethylene butylene)-*block*-polystyrene-*block*-poly(ethylene butylene) tetrablock copolymer with a weight fraction of polystyrene (PS) of 0.205, which displays spherical morphology. The measurements are carried out at high temperatures between the glass transition temperature of PS and the order–disorder transition temperature ($T_{ODT} \sim 190°C$) of the block copolymer under uniaxial elongation with $\dot{\epsilon}_0$ between 0.01 and 1.0 s^{-1}. The data exhibit strain-induced softening under high $\dot{\epsilon}_0$ ($\sim 1.0\ s^{-1}$) at low temperatures, but strain-induced hardening under low $\dot{\epsilon}_0$ ($\sim 0.01\ s^{-1}$) at high temperatures. The stress-optical coefficient $C(\dot{\epsilon}_0; t)$ is almost constant under high $\dot{\epsilon}_0$ at low temperatures, close to the value of low-density polyethylene melt ($\sim 2.2 \times 10^{-9}\ Pa^{-1}$), whereas it increases by approximately 10–50 times under low $\dot{\epsilon}_0$ at high temperature. The plots of the $C(\dot{\epsilon}_0; t)$ vs. t/a_T (a_T being the WLF shift factor) are roughly fitted into a single curve, indicating that the $C(\dot{\epsilon}_0; t)$ depends on t/a_T, rather than Hencky strain ϵ. Such behavior, especially under low $\dot{\epsilon}_0$, reflects the contribution of *form* birefringence Δn_f of the deformed PS domains. Small angle X-ray scattering and transmission electron microscopy observation reveal that under high $\dot{\epsilon}_0$, the spherical PS-domains are not appreciably changed, whereas under low $\dot{\epsilon}_0$, they are deformed into cylinders and oriented along the direction of elongation, thereby resulting in the large contribution of Δn_f.

Keywords: Elongational flow; Tensile viscosity; Birefringence

1. Introduction

Combination of rheometry and internal structure analysis has been found remarkably successful in the studies on the dynamic structures of homopolymer melts and multiphase polymer systems such as semicrystalline polymer liquids, polymer blends and block copolymers [1]. Rheo-optical techniques were particularly useful in characterizing structure development induced by a flow field [2,3]. In recent years much attention has been paid to application of the combined rheometry–structure analysis approach to the study on block copolymers with certain distinct microdomain structures. Keller et al. [4,5] firstly used melt extrusion for polystyrene-*block*-polybutadiene-*block*-polystyrene (SBS) triblock copolymer melt and demonstrated a dramatic alignment of polystyrene (PS) cylinders into a well-ordered hexagonally packed structure. The application of a hydrodynamic flow field has been proven effective in inducing morphological orientation in block copolymer melts. Hadziioannou et al. [6] also reported that a large-amplitude oscillatory shear led to the flow-induced alignment of lamellae in a block copolymer melt parallel to the shearing plane. More recently, it was reported that a shear flow also induced the orientation of cylindrical domains in block copolymer melts [7–16]. Especially, Koppi et al. [10] found that the lamellar phase of poly(ethylene propylene)-*block*-poly(ethyl ethylene) (PEP–PEE) diblock copolymer showed a flipping transition under oscillatory shear flow, where the lamellar normals rotated from the shear gradient to the

* Corresponding author. Tel.: +81-52-809-1860; fax: +81-52-809-1864.
E-mail address: kotaka@toyota-ti.ac.jp (T. Kotaka).

[1] Present address. Toray Industry Ltd., Ooe-cho 9-1, Minatoku, Nagoya 455-8502, Japan.

0032-3861/01/$ - see front matter
PII: S0032-3861(00)00422-5

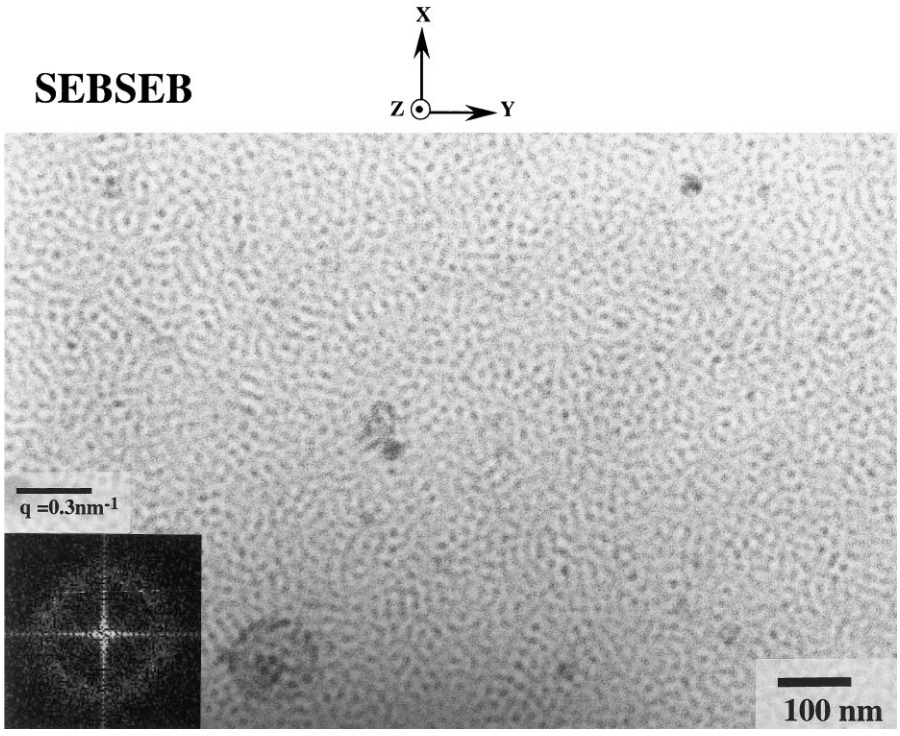

Fig. 1. TEM micrograph showing the *xy*-plane of the initial SEBSEB film. The insert shows its computed FFT image.

vorticity axis near the order–disorder transition temperature (T_{ODT}) or at high shear rate. The flipping transition was also reported for a number of diblock copolymer systems [12–16]. Recently, elongation behavior of block copolymer melts was reported by Takahashi et al. [17] on an SBS triblock copolymer with lamellar morphology. However, rheo-optical studies on block copolymer melts under elongational flow are still sparse.

To address the need for direct monitoring of the local segmental orientation and mechanical response of polymer melts under elongational flow, we recently constructed a new technique of elongational flow opto-rheometry (EFOR) which enabled us to make simultaneous measurements of transient tensile stress $\sigma(\dot{\epsilon}_0; t)$ and birefringence $\Delta n(\dot{\epsilon}_0; t)$ of polymer melts as a function of time t under uniaxial elongation at a constant Hencky strain rate $\dot{\epsilon}_0$ [18]. We demonstrated that the stress-optical rule (SOR) [19,20] was well obeyed for homopolymer melts [18,21,22] and miscible polymer blends [23] even during high strain-rate elongation. However, the SOR was invalid for complex polymeric liquids with deformable microdomains of different refractive indices such as supercooled semicrystalline polymer liquids [24–28] and immiscible polymer blends [29].

In this paper we describe the results of the EFOR study on the elongation behavior of a tetrablock copolymer melt of polystyrene-*block*-poly(ethylene butylene)-*block*-polystyrene-*block*-poly(ethylene butylene) (SEBSEB) between the glass transition of PS domains ($T_{g(PS)}$), ~100°C and T_{ODT}, ~190°C. Small angle X-ray scattering (SAXS) and transmission electron microscopy (TEM) are also used to investigate the morphological change and deformation of the SEBSEB melt during elongation.

2. Experimental

2.1. Material

A laboratory grade SEBSEB tetrablock copolymer sample was kindly supplied by Asahi Chemical Co. According to the supplier, the sample was derived by attaching a short segment of the PEB block ($M_n = 2$ kg mol^{-1}) to either end of a precursor symmetric polystyrene-*block*-poly(ethylene butylene)-*block*-polystyrene (SEBS) triblock copolymer, which was the Asahi Chemical's laboratory grade sample having a PS weight fraction of 0.209. The weight- (M_w) and number-average molecular (M_n) weights were 72.6 and 66.0 kg mol^{-1}, respectively, determined by gel permeation chromatography (GPC) using a PS elution standard. The characteristics of the SEBSEB sample were the following: a PS weight fraction was 0.205, M_n was 68.0 kg mol^{-1}, polydispersity index was approximately 1.1 and block sequence in M_n was 6.9–52.2–6.9–2.0 (kg mol^{-1}). The GPC result showed that it contained a small amount (less than 3 wt%) of a high M_n (~136 kg mol^{-1}) component. However, the sample was used without removing the high M_n trace. The melt flow index (MFR) at 230°C under 2.16 kgw load was 5.3 (g/10 min), and the T_{ODT} (~190°C) was determined from temperature dependence of the isochronal dynamic moduli.

2.2. Sample preparation

Preparation of a molded SEBSEB sheet was carried out as follows. As-received pellets were placed between polyimide films (Kapton® HN, Toray-Du Pont) and compression-molded at 5 MPa for 6 min with a laboratory hot-press kept at 260°C, which was higher than the T_{ODT} of the SEBSEB sample. The molded sheet with a thickness in the range of 1.8–2.0 mm was transferred to another hot-press kept at ambient temperature without applying load, and then annealed by circulating water into the jacket of the hot-press to form a fully phase-separated domain structure. The sheet was cut into strips of approximately $60 \times 7.0 \times (1.8–2.0)\ mm^3$ in size and subjected to the EFOR and SAXS measurements.

2.3. Refractive indices

To check the optical anisotropy of the as-prepared SEBSEB film before elongation, we examined its birefringence under quiescent state at room temperature by using a three-dimensional birefringence analyzer (KOBRA-21DH; Oji Scientific Instruments Co.). We measured refractive indices, n_x, and n_y, along the arbitrarily chosen orthogonal x- and y-axes of the specimen surface and n_z along the z-axis direction perpendicular to the surface (see Fig. 1).

2.4. TEM

The morphologies of the unelongated and elongated SEBSEB films were observed by TEM (EM H-300, Hitachi Co.), operated at an acceleration voltage of 100 kV. Measurements were carried out at Tokyo Institute of Technology. The ultrathin sections of the SEBSEB sample were obtained under cryogenic condition in a Reichert Ultracut N/SC4E at −100°C, below the glass transition temperature $T_{g(PEB)}$ (approximately −70°C) of the PEB block and then stained with an RuO_4 vapor at 50°C for 2 h. A fast Fourier transform (FFT) analysis was carried out on the digitally saved images of the TEM micrographs using a commercial image analysis software (Ultimage®; Graftek France).

2.5. SAXS

The SAXS measurements were conducted to analyze the domain structure of the SEBSEB samples. Measurements were made at JAIST with CuK_α radiation (wavelength $\lambda =$ 0.1542 nm) generated from a 18 kW rotating anode generator (MAC Science M18X) operated at 40 kV and 30 mA. Angular dependence of the SAXS intensities was monitored with a point-focusing optics and a one-dimensional position sensitive proportional counter of the effective length of 100 mm. The data were usually collected for 50 min. For this point focusing optics, the correction for slit-width smearing was not needed due to the finite cross section of the primary beam [30]. The details were described elsewhere [31].

In these measurements, the samples were prepared in the following way. The elongated sample, just after the EFOR measurement, was rapidly quenched by placing between cold metal plates to freeze the internal microdomain structures developed during elongation. Then, the center portion of the elongated film was cut into several pieces with a thickness of ca 1 mm and subjected to the SAXS measurement. For the elongated SEBSEB films, the SAXS scans were made in the directions parallel (x-axis) and perpendicular (y-axis) to the elongation direction. All the SAXS measurements were performed at room temperature.

2.6. EFOR

Simultaneous measurements of transient tensile stress $\sigma(\dot{\epsilon}_0; t)$ and birefringence $\Delta n(\dot{\epsilon}_0; t)$ were conducted on our recently developed EFOR [18], such as a Meissner's new elongational rheometer [32] (commercialized as RME from Rheometric Scientific) combined with a birefringence optics. In each EFOR run the specimen was held for 90 s at a desired temperature prior to the EFOR run. At each temperature the runs were carried out with three different Hencky strain rates $\dot{\epsilon}_0$ of 0.01, 0.1 and 1.0 s^{-1}. In these measurements the samples were set to be stretched along the x-axis direction.

The tensile force and retardation were directly measured in each EFOR run. Tensile stress, $\sigma(\dot{\epsilon}_0; t)$, was calculated by dividing the force by the cross sectional area $A(\dot{\epsilon}_0; t)$ of the specimen under elongation. For the calculation of the birefringence $\Delta n(\dot{\epsilon}_0; t)$, the thickness $d(\dot{\epsilon}_0; t)$ data were needed. Assuming no volume change during elongation, the $A(\dot{\epsilon}_0; t)$ and $d(\dot{\epsilon}_0; t)$ were calculated from the initial dimensions, $A(\dot{\epsilon}_0; t)$ and $d(\dot{\epsilon}_0; t)$ of the specimen at each temperature, which were in turn estimated from the actually measured dimensions at the ambient temperature.

We also assumed the additivity of the specific volumes and employed reported thermal expansivity data of the component homopolymers. Then the specific volume $\bar{v}_{SEB}$ of the block copolymer can be expressed as

$$\bar{v}_{SEBSEB} = w_{PS}\bar{v}_{PS}(T) + w_{PEB}\bar{v}_{PEB}(T) \quad (1)$$

where w_{PS} and w_{PEB} are the weight fractions and $\bar{v}_{PS}(T)$ and $\bar{v}_{PEB}(T)$ are the specific volumes of the PS and PEB blocks, respectively, at a certain temperature. In these approximations, we employed the literature data of PS density [33] at various temperatures and the specific volume data of amorphous low-density polyethylene (LDPE) for the PEB blocks [34]:

$$\bar{v}_{LDPE}(T) = 1.262 + 0.0009 \times (T - 125) \quad (2)$$

The specimen showed a weak birefringence even in a quiescent state. The difference between the intensities of S_p (+45° inclination to the stretching direction) and S_s (−45° inclination to the stretching direction) components of the specimen was offset prior to the EFOR run and the time evolution of the birefringence $\Delta n(\dot{\epsilon}_0; t)$ was then measured [18].

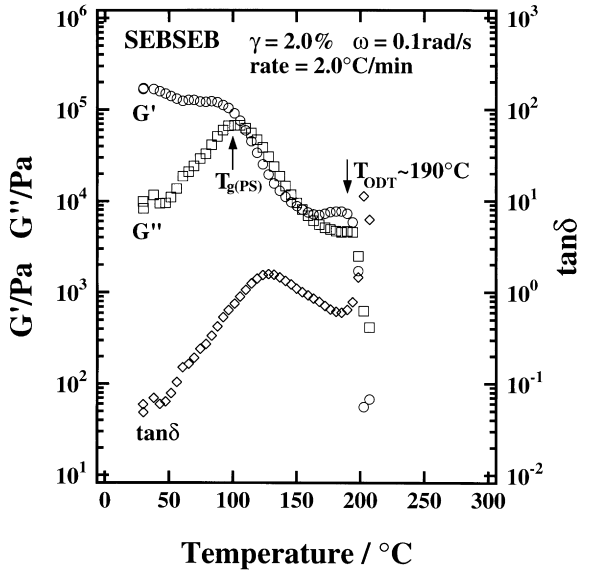

Fig. 2. Temperature dependence of G', G'' and tan δ of the SEBSEB melt under isochronal condition at $\omega = 0.1$ rad s^{-1} and $\gamma = 2.0\%$, measured during heating at a heating rate of 2°C min^{-1}.

2.7. Dynamic mechanical analysis

Dynamic mechanical analysis was conducted on a conventional rheometer (RDAII, Rheometric Scientific, USA) with a parallel-plate geometry of 25.0 mm diameter. To monitor the temperature dependence of the complex moduli, we operated the rheometer in an oscillatory shear mode under isochronal condition at a fixed angular frequency of $\omega = 0.1$ rad s^{-1} and a strain amplitude of $\gamma = 0.2\%$ to avoid complication due to the nonlinear response of the sample. The T dependence of dynamic G', loss G'' moduli and their ratios, $G'/G'' = \tan\delta$, were determined between 30 and 220°C.

Dynamic frequency sweep tests were conducted also on RDA II at various temperatures between 130 and 170°C. The ω was varied from 0.1 to 100 rad s^{-1} and the γ was adjusted from 0.2 up to 10% to obtain reasonable signal intensities even at elevated temperatures or low frequencies by avoiding the nonlinear response as much as possible.

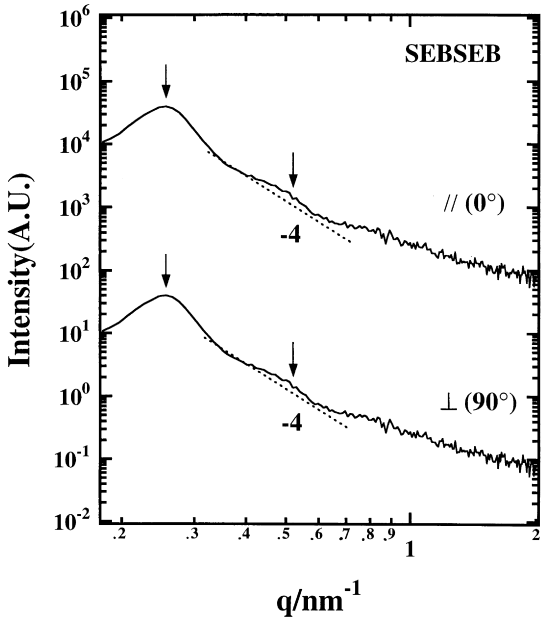

Fig. 3. SAXS data of the unelongated SEBSEB film, measured in the x- and y-axes directions, where the data in the y-axis direction was shifted by a factor of 10^{-3} to avoid the data overlap. The dashed line represented $I(q) \sim q^{-4}$.

3. Results

3.1. Characterization of the as-prepared film

3.1.1. Refractive indices

Refractive indices at 25°C were found to be 1.53402, 1.53401 and 1.53396 for n_x, n_y and n_z, respectively, for which the coordinates were taken as shown in Fig. 1. The difference between n_x and n_y was negligible (in the order of 10^{-5}), whereas the differences $\Delta n_{fyz}(= n_y - n_z)$ and $\Delta n_{fzx}(= n_z - n_x)$ were positive and negative, respectively, with almost the same absolute magnitude of the order of 5×10^{-5}. The negative value of Δn_{fzx} was expected from the values of the refractive indices of the homopolymers PS (~1.59) and PEB (~1.50) [35]. It is likely that the intrinsic anisotropy of the PS domains in the unelongated SEBSEB specimen is negligible because of the random arrangement of the PS domains.

3.1.2. TEM micrographs

A typical micrograph of the specimen prior to elongation was shown in Fig. 1. In this measurement, an ultrathin film of the SEBSEB sample was prepared by quenching from the melt at 260°C, far above its T_{ODT}, and held at room temperature for additional days prior to observation. In Fig. 1, the dark areas represent the PS domains stained with RuO_4, which are surrounded by the distorted, bright PEB matrix, suggesting the existence of the disordered spherical phase.

The insert in Fig. 1 was an FFT image of the digitized TEM micrograph. In this image, only an isotropic diffuse halo was observed with a maximum intensity centered at $q[= (4\pi/\lambda)\sin(\theta/2)$, where θ and were scattering angle and wavelength used in the FFT calculation] of ~0.25 nm^{-1}. It appeared due to the disordered PS spheres with a domain spacing (d) of approximately 25 nm. The halo in the FFT image indicated that the disordered microdomains of the PS spheres were randomly arranged in the PEB matrix.

3.1.3. Viscoelastic responses

Fig. 2 shows changes of the dynamic (G') and loss (G'') moduli and the ratio ($G'/G'' = \tan\delta$) of the molded SEBSEB sheet, as a function of temperature in the range of $30 \le T \le 220$°C. A heating rate of 2°C min^{-1} was used in

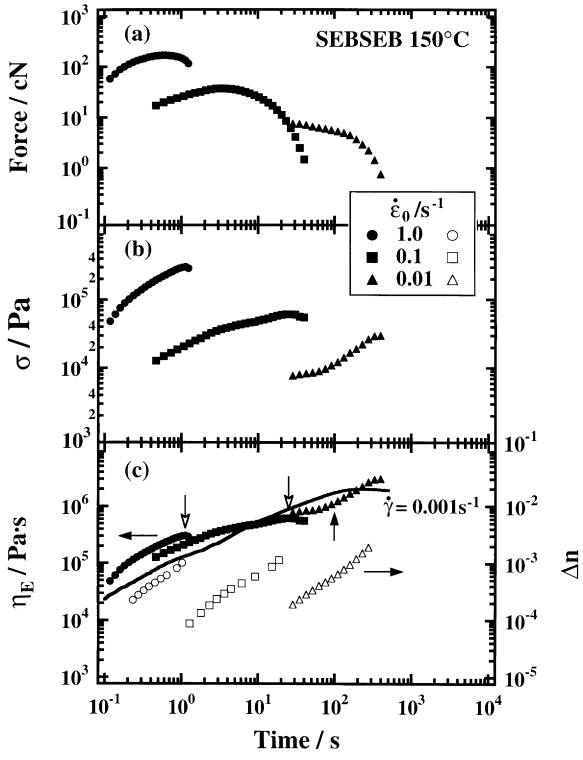

Fig. 4. Double logarithmic plots of the: (a) tensile force $F(\dot{\epsilon}_0;t)$; (b) tensile stress $\sigma(\dot{\epsilon}_0;t)$; and (c) elongational viscosity $\eta_E(\dot{\epsilon}_0;t) \equiv \sigma(\dot{\epsilon}_0;t)/\dot{\epsilon}_0$ (closed symbols) and $\Delta n(\dot{\epsilon}_0;t)$ (open symbols) vs. time of the SEBSEB melt elongated at 150°C with three different $\dot{\epsilon}_0$. The solid line in (c) shows $3\eta_0(\dot{\gamma};t)$, measured at a low shear rate $\dot{\gamma} = 0.001\ s^{-1}$ in a cone-plate rheometer.

this measurement. In Fig. 2, both G' and G'' showed a rapid decrease near 190°C, indicating the existence of the T_{ODT} of the SEBSEB as previously reported by Rosedale et al. [36]. In both data, there was another change near 100°C, which corresponded to the T_g of the PS blocks.

3.1.4. SAXS

Fig. 3 shows the corrected SAXS scans of the unelongated SEBSEB film along the *x*- and *y*-axes, taken on the film surface. The data showed the double logarithmic plots of the relative scattered intensities $I(q)$ vs. the scattering vector, $q = (4\pi/\lambda)\sin(\theta/2)$, where λ and θ were the wavelength of the X-ray and scattering angle, respectively.

Both scan data in Fig. 3 are almost the same, indicating the microdomain structures of the PS and PEB blocks are isotropic. In these scans, we found a broad first-order peak at $q \sim 0.26\ nm^{-1}$ and weak second-order peak at $q \sim 0.51\ nm^{-1}$. The broadness of the peaks was due to the fact that the spherical domains were rather disordered and short-range ordered. The domain spacings corresponding to the first-order maximum peaks of both scans were estimated as 24.6 nm, close to one measured in the FFT image of the TEM micrograph. The decay of the SAXS intensities in the q range from 0.35 to 0.6 nm^{-1} can be expressed by a power law in the form $I(q) \cong q^{-4}$, suggesting that the sharp interfaces with a finite thickness exist even in the disordered spherical phase [37].

3.2. Elongation of the film in the melt state

3.2.1. Elongational viscosity

Fig. 4 shows double logarithmic plots of the: (a) tensile force $F(\dot{\epsilon}_0;t)$; (b) tensile stress $\sigma(\dot{\epsilon}_0;t) \equiv F(\dot{\epsilon}_0;t)/A(\dot{\epsilon}_0;t)$; and (c) elongational viscosity $\eta_E(\dot{\epsilon}_0;t)$ and birefringence $\Delta n(\dot{\epsilon}_0;t)$ of the SEBSEB film vs. elongation time, t, at 150°C. Fig. 5 shows plots of the $\eta_E(\dot{\epsilon}_0;t)$ and the $\Delta n(\dot{\epsilon}_0;t)$ vs. t of the SEBSEB sample elongated at four different temperatures between $T_{g(PS)}$ and T_{ODT}. In these measurements three different $\dot{\epsilon}_0$ (0.01, 0.1 and 1.0 s^{-1}) were used at each temperature.

In Fig. 4(a), the $F(\dot{\epsilon}_0;t)$ with $\dot{\epsilon}_0$ gradually decreased with time, while those with $\dot{\epsilon}_0$ and 1.0 s^{-1} displayed an initial increase, followed by a gradual decrease with t. During elongation with the highest rate $\dot{\epsilon}_0$ the melt abruptly ruptured at $t = 1.2\ s$ or $\epsilon = 1.2$, far below the maximum attainable Hencky strain of $\epsilon = 7$. In Figs. 4(b) and (c) and 5, the changes in $\sigma(\dot{\epsilon}_0;t)$ and $\eta_E(\dot{\epsilon}_0;t)$ with t were rather complicated with the $\dot{\epsilon}_0$. In these figures, the $\eta_E(\dot{\epsilon}_0;t)$ measured at three different $\dot{\epsilon}_0$ did not show any linear region where $\eta_E(\dot{\epsilon}_0;t)$ was independent of $\dot{\epsilon}_0$. In Fig. 4(c), they were compared with the three-fold shear viscosity, $3\eta_0(\dot{\gamma};t)$, with a constant shear rate of $\dot{\gamma} = 0.001\ s^{-1}$ at 150°C. The extended Trouton rule, $3\eta_0(\dot{\gamma};t) \cong \eta_E(\dot{\epsilon}_0;t)$ [38] did not hold for the SEBSEB melt.

In Figs. 4(c) and 5, the $\eta_E(\dot{\epsilon}_0;t)$ with $\dot{\epsilon}_0 = 0.01\ s^{-1}$ increased rather rapidly at the up-rising time $t^{up}_{\eta_E}$, marked with the upward arrow, but one with higher $\dot{\epsilon}_0$ (0.1 or 1.0 s^{-1}) decreased at the down-descending time $t^{down}_{\eta_E}$, marked with the downward arrows. The upward deviation of the $\eta_E(\dot{\epsilon}_0;t)$ implying the strain-induced hardening became prominent below $\dot{\epsilon}_0 = 0.01\ s^{-1}$ and above 160°C, while the downward deviation, associated with the strain-induced softening, became prominent at high $\dot{\epsilon}_0$ (0.1 and 1 s^{-1}) and at low temperatures (130 and 150°C). These results seemed opposite to ordinary homopolymer melts, for which the strain-induced hardening usually occurred at high $\dot{\epsilon}_0$ and low temperature [18]. On elongation of homopolymer melts, the upward deviation of the $\eta_E(\dot{\epsilon}_0;t)$ takes place at a common Hencky strain $\epsilon_{\eta_E} = (\dot{\epsilon}_0 t_{\eta_E} \sim \text{constant})$, which is almost insensitive to either strain rate $\dot{\epsilon}_0$ or temperature of elongation.

3.2.2. Birefringence

Figs. 4(c) and 5 show the $\Delta n(\dot{\epsilon}_0;t)$ of the SEBSEB melt measured at different temperatures and $\dot{\epsilon}_0$. The data measured just before rupture were not included in this figure because the dimensions of the specimens were enormously changed during elongation and their corresponding $\Delta n(\dot{\epsilon}_0;t)$ could not be measured precisely.

The plots of $\Delta n(\dot{\epsilon}_0;t)$ vs. t displayed that the sign of the retardation or the $\Delta n(\dot{\epsilon}_0;t)$ was always positive in the early

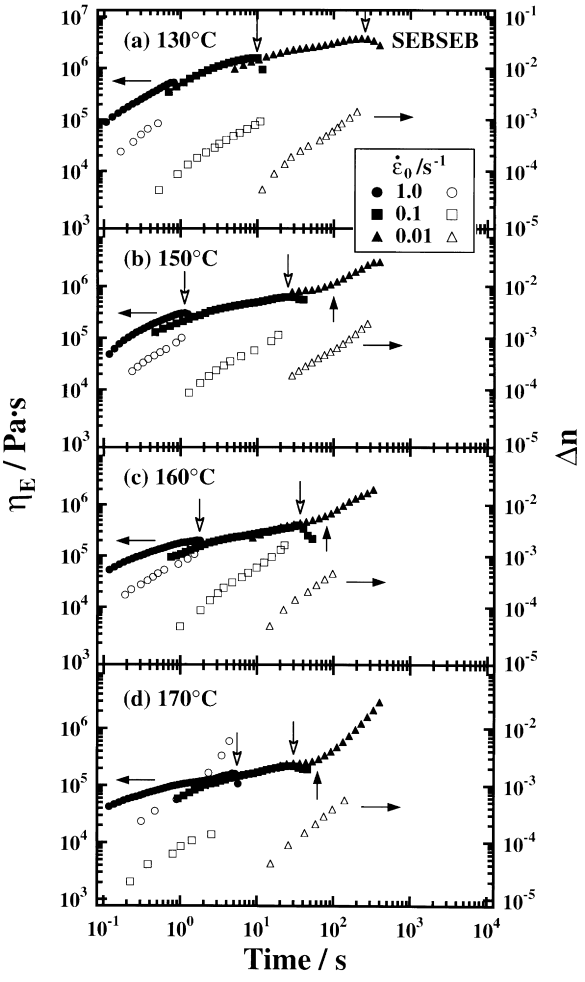

Fig. 5. Time dependence of the elongational viscosity $\eta_E(\dot{\epsilon}_0;t)$ and $\Delta n(\dot{\epsilon}_0;t)$ of the SEBSEB melt at various temperatures with different $\dot{\epsilon}_0$. The upward (closed) and downward (open) arrows indicate the up-rising time $t_{\eta_E}^{up}$ and down-descending time $t_{\eta_E}^{down}$, respectively.

stage of the EFOR runs. Because the SEBSEB chain is composed of PS and PEB segments with different signs of Δn, i.e. positive for the PEB block and negative for the PS block, the positive sign of Δn in the early stage implies a preferential elongation of the PEB matrix. In Fig. 5, the $\Delta n(\dot{\epsilon}_0;t)$ of the SEBSEB melt increased linearly with t in the first stage, but followed by a gradual decrease on continuous elongation. These data implied that the continuous, soft PEB matrix was initially elongated in the beginning, which caused the elongation and distortion of the discontinuous PS domains on further elongation.

3.3. SOR for the SEBSEB melt

3.3.1. Effect of strain rate

The SOR is a simple law that states a simple proportionality between the refractive index and the anisotropic stress tensors [19,20]. Doi and Edwards [20] described that the SOR is based on two essential assumptions: (a) the orientation of the bond vectors has a linear relationship with that of

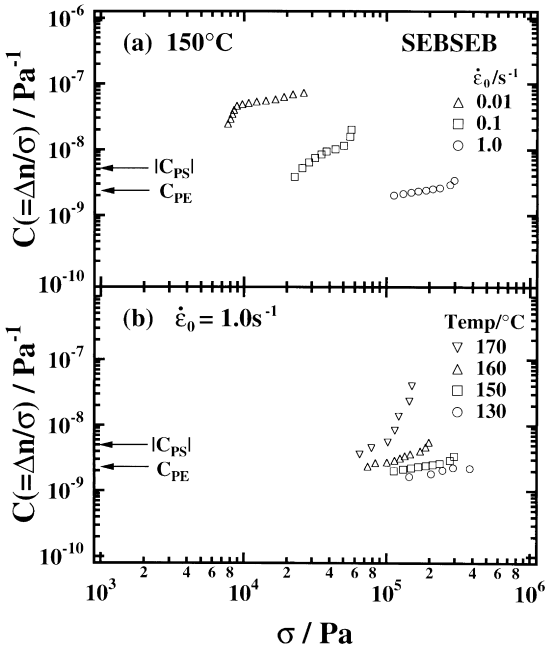

Fig. 6. Double logarithmic plots of the: (a) $C(\dot{\epsilon}_0;t)(\equiv \Delta n(\dot{\epsilon}_0;t)/\sigma(\dot{\epsilon}_0;t))$ vs. $\sigma(\dot{\epsilon}_0;t)$ at 150°C; and (b) $C(\dot{\epsilon}_0;t)$ vs. $\sigma(\dot{\epsilon}_0;t)$ with $\dot{\epsilon}_0 = 1.0\ s^{-1}$ at various temperatures. The arrows point out the values of $|C_{PS}(\dot{\epsilon}_0;t)|(= 5.2\times10^{-9}\ Pa^{-1})$ for PS and $C_{PE}(\dot{\epsilon}_0;t)(= 2.2\times10^{-9}\ Pa^{-1})$ for LDPE melt measured during elongation [18].

the end-to-end vector of the Rouse segments; and (b) the form birefringence is neglected. For ordinary homopolymer melts, both assumptions are valid. However, the form birefringence cannot be neglected for block copolymer melts and polymer blends having phase-separated domain morphologies. For the elongation of homopolymer melt, the rule describes:

$$\Delta n(\dot{\epsilon}_0;t) = C(\dot{\epsilon}_0;t)\sigma(\dot{\epsilon}_0;t) \tag{3}$$

where $C(\dot{\epsilon}_0;t)$ is the stress optical coefficient, first given by Treloar et al. [39] for rubber elasticity, and is independent of not only $\epsilon(=\dot{\epsilon}_0 t)$ or $\sigma(\dot{\epsilon}_0;t)$ but also $\dot{\epsilon}_0$ as long as the SOR holds.

Fig. 6(a) shows the double logarithmic plots of $C(\dot{\epsilon}_0;t)[\equiv \Delta n(\dot{\epsilon}_0;t)/\sigma(\dot{\epsilon}_0;t)]$ vs. $\sigma(\dot{\epsilon}_0;t)$. The reported values of $C(\dot{\epsilon}_0;t)$ of PS and LDPE melts [18,21,22] are also shown for comparison. In this figure the changes in $C(\dot{\epsilon}_0;t)$ at three $\dot{\epsilon}_0$ were different. On elongation of the SEBSEB melt, especially below its T_{ODT}, $\Delta n(\dot{\epsilon}_0;t)$ was no longer proportional to $\sigma(\dot{\epsilon}_0;t)$ and the SOR did not seem to hold. The $C(\dot{\epsilon}_0;t)$ measured during elongation with $\dot{\epsilon}_0 = 1.0\ s^{-1}$ increased gradually with $\sigma(\dot{\epsilon}_0;t)$ above the value of the $C_{PE}(\dot{\epsilon}_0;t)$ $(=2.2\times10^{-9}\ Pa^{-1})$ of LDPE melt, whereas that for the $\dot{\epsilon}_0 = 0.01\ s^{-1}$ rapidly increased in the early stage, followed by a gradual increase with $\sigma(\dot{\epsilon}_0;t)$. The $C(\dot{\epsilon}_0;t)$ was higher than that $(=-5.2\times10^{-9}\ Pa^{-1})$ of PS melt at large elongation, which deviated from values expected by the SOR.

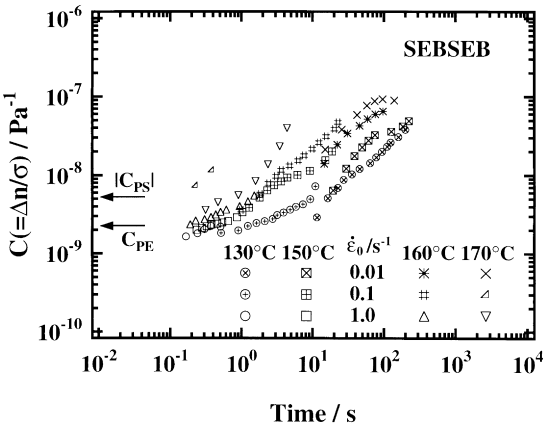

Fig. 7. Double logarithmic plots of $C(\dot{\epsilon}_0;t)$ vs. t at various temperatures with different $\dot{\epsilon}_0$. The solid and open arrows represent the $t_{\eta_E}^{up}$ and $t_{\eta_E}^{down}$, respectively.

3.3.2. Effect of temperature

Fig. 6(b) shows the plots of the $C(\dot{\epsilon}_0;t)$ vs. $\sigma(\dot{\epsilon}_0;t)$ for the SEBSEB melt with $\dot{\epsilon}_0$ at four different temperatures. The $C(\dot{\epsilon}_0;t)$ displayed a rapid increase above 160°C. It showed a gradual increase in the elongation at 130 and 150°C, starting approximately from the level of the $C_{PE}(\dot{\epsilon}_0;t)$ of LDPE melt. The enormous deviation of the $C(\dot{\epsilon}_0;t)$ from the values expected by the SOR was found at a low $\dot{\epsilon}_0$ at high temperature, while one measured with a high $\dot{\epsilon}_0$ at low temperature gave a slight deviation. These deviations were mostly due to the contribution of the form birefringence Δn_f of the deformed PS domains which was prominent with low $\dot{\epsilon}_0$ at high temperatures.

Fig. 6 can be redrawn roughly into a single composite curve by plotting against t instead of σ, as seen in Fig. 7. The $C(\dot{\epsilon}_0;t)$ became larger at high temperature and its increase reflects the decrease in $\sigma(\dot{\epsilon}_0;t)$ or increase in $\Delta n(\dot{\epsilon}_0;t)$ due to the contribution of the Δn_f of the PS microdomains at high temperatures under slow elongation.

3.4. Structure of the elongated melt

3.4.1. TEM micrographs

Fig. 8 shows TEM micrographs of the quenched melts after elongation at 150°C up to: (a) $\epsilon = 2.2$ ($\lambda = 8.9$) with $\dot{\epsilon}_0 = 1.0\ s^{-1}$; and (b) $\epsilon = 4.9$ ($\lambda = 134.3$) with $\dot{\epsilon}_0 = 0.01\ s^{-1}$. The specimens were prepared from the melts by quenching with water and keeping at room temperature for overnight in a dried condition. Fig. 8(a) shows almost the same features as those seen in Fig. 1. Although shown in low

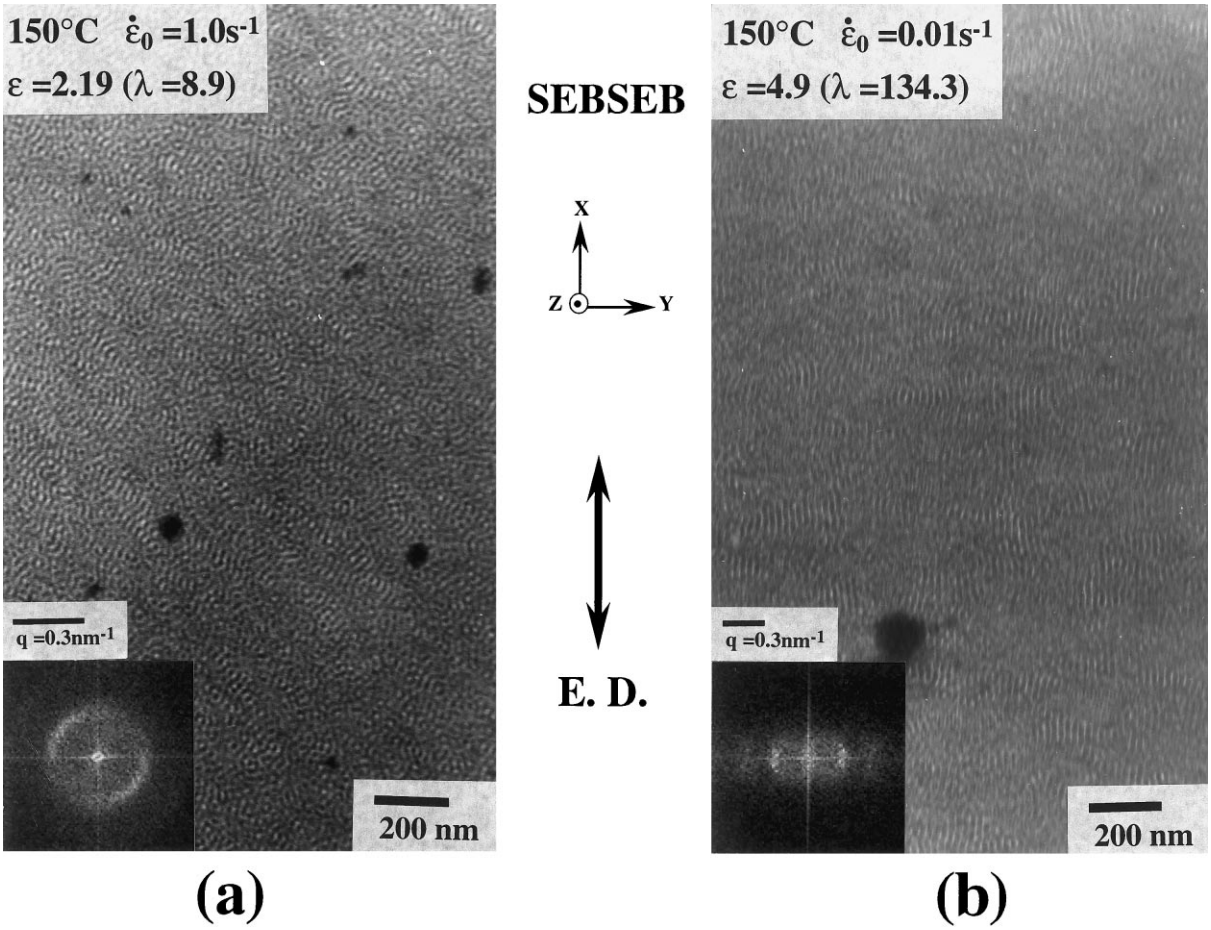

Fig. 8. TEM micrographs in the xy plane of the SEBSEB melt, elongated at 150°C with: (a) $\dot{\epsilon}_0 = 1.0\ s^{-1}$ up to $\epsilon = 1.89$ ($\lambda = 6.6$); and (b) $\dot{\epsilon}_0 = 0.01\ s^{-1}$ up to $\epsilon = 4.9$ ($\lambda = 134.3$). The inset displays a computed FFT spectrum of the micrograph.

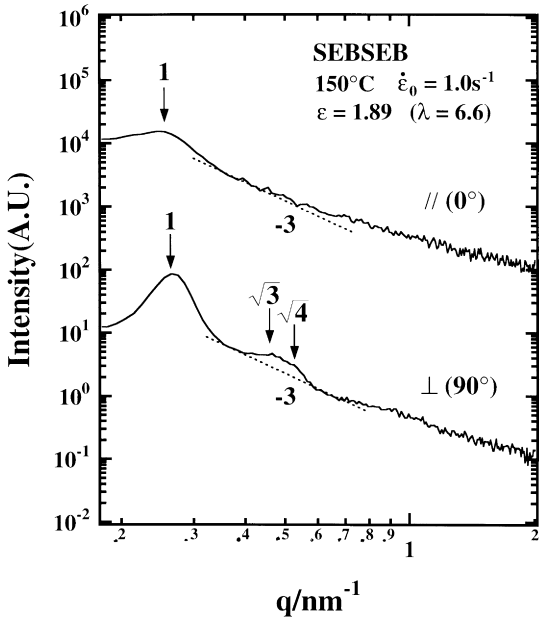

Fig. 9. SAXS data of the SEBSEB melt, elongated at 150°C with $\dot{\epsilon}_0 = 1.0\ s^{-1}$ up to $\epsilon = 1.89$ ($\lambda = 6.6$) in the direction: (a) parallel (0° or *x*-axis); and (b) perpendicular (90° or *y*-axis) to the elongation direction. The data shown in (b) were vertically shifted by a factor of 10^{-3} to avoid data overlap. The dashed line represents $I(q) \sim q^{-3}$.

magnification, the initial, disordered spherical domains were distorted by elongation, and inclined to the elongated direction in localized areas. It was confirmed by the FFT image of the TEM micrograph, shown in the insert of Fig. 8(a), displaying the broad scattered intensities centered at approximately −45 and 135°, overlapped with a diffuse halo.

Fig. 8(b) shows the TEM micrograph of the SEBSEB melt quenched from the melt elongated by $\epsilon = 4.9$ ($\lambda = 134.3$) with $\dot{\epsilon}_0 = 0.01\ s^{-1}$, well above the point ($\epsilon \sim 1.0$) where the strain-induced hardening starts. In this figure, the dark PS domains were mostly aligned to the elongation direction. The FFT image, shown in the insert in Fig. 8(b), also displayed two peak intensities on the equator, such as the direction perpendicular to the elongation. The domain spacing ($d_\perp$) estimated from both the TEM micrograph and the FFT image was approximately 22 nm which was reduced, as compared with the value (24.7 nm) of the unelongated film.

3.4.2. SAXS

Fig. 9 shows the SAXS scans obtained from the SEBSEB melt elongated by $\epsilon = 1.89$ (stretch ratio $\lambda = 6.6$) with $\dot{\epsilon}_0 = 1.0\ s^{-1}$ at 150°C, beyond the onset of the strain-induced softening, measured in the direction parallel (∥) (top) and perpendicular (⊥) (bottom) to the elongation direction. The samples were prepared in the same way as described in the previous TEM measurement. In Fig. 9, a broad peak appeared at $q \sim 0.25\ nm^{-1}$ in the parallel (∥) scan data without additional higher order peak intensities, whereas a relatively intense peak intensity was found at $q \sim 0.26\ nm^{-1}$ and an additional peak was also observed around $q \sim 0.5\ nm^{-1}$ in the perpendicular (⊥) scan data.

The difference between both data implied that the elongated SEBSEB melt became anisotropic. However, the existence of the peak at around $q \sim 0.25\ nm^{-1}$ in both scan data indicated that the preexisting spherical domains still remained in the elongated structure. However, the improved peak sharpness and intensity of the main peak in the perpendicular (⊥) scan data may be due to the coexistence of the anisotropic phase with the disordered spherical phase. A closer investigation on the peak at $q \sim 0.5\ nm^{-1}$ revealed the implication of the existence of double peaks at $q \sim 4.6$ and $5.3\ nm^{-1}$. The intense main peak and the implication of the double peaks around the second-order peak reveals the existence of the anisotropic cylindrical phase, packed in a two-dimensional hexagonal lattice.

Assuming that the scattered X-ray intensities in the range of $0.35 \leq q \leq 0.6\ nm^{-1}$ in Fig. 9 show the power-law-type decay [$I(q) \cong q^{-n}$], the approximate roughness of the interface between the PS and PEB blocks can be estimated by the value of exponent *n*, as approximately 3. As compared with one for the unelongated SEBSEB melt, such as approximately 4, the decrease in the *n* value during elongation might be due to the distorted and roughened interfacial structure of the elongated SEBSEB melt [40]. However, the positions of the first-order peaks of Figs. 3 and 9 were not changed much during elongation: $q = 0.26\ nm^{-1}$ ($d = 24.6$ nm) for the unelongated melt; $q_\parallel = 0.25\ nm^{-1}$ ($d_\parallel = 24.7$ nm) and $q_\perp = 0.26\ nm^{-1}$ ($d_\perp = 23.8$ nm) (where $q_\parallel$ and $q_\perp$ were the scattering vectors measured in the directions parallel and perpendicular to the elongation directions; $d_\parallel$ and $d_\perp$ were the corresponding *d*-spacing values, respectively). The SAXS data of the highly elongated melts could not be made in the present experiment because the specimen became too thin to be measured.

4. Discussion

4.1. Morphological change during elongation

The SAXS data of the elongated SEBSEB film confirmed that the structural anisotropy was developed on the elongation. The increased peak intensity and sharpness may be due to the development of the anisotropic cylindrical phase during elongation. It was confirmed by the TEM micrograph, shown in Fig. 8, displaying the existence of the layered domains in the localized regions which were also inclined to the stretching direction. The inclination of the domains during elongation with high $\dot{\epsilon}_0$ at low temperature may be caused by a slippage of the short-range ordered domains or their local rearrangement. In such case, the domain spacing in the direction perpendicular ($d_\perp$) and parallel ($d_\parallel$) to the elongation direction remains almost constant. During elongation, the interface roughness might

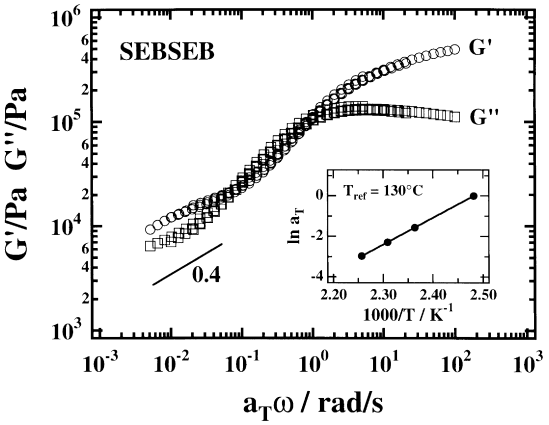

Fig. 10. The plots of G' and G'' vs. the reduced frequency $a_T\omega$ plots of the SEBSEB melt with the reference temperature $T_{ref} = 130°C$. The shift factors a_T were plotted in the inset and the shifted data showed the slope 0.4 in the low-ω region. The solid line represents the fit with an Arrhenius-type equation.

be increased by the deformation or distortion of the domains.

On elongation up to $\lambda = 134.3$ (or $\epsilon = 4.9$) with $\dot{\epsilon}_0 = 0.01\ s^{-1}$ at 150°C, the spacing $d_\perp$ was reduced from approximately 25 to 20 nm, implying that the imposed tensile stress effectively deformed both PS and PEB domains and displayed the strain-induced hardening behavior. These results also pointed out that the elongation with low $\dot{\epsilon}_0$ might suppressed the early rupture of the specimens, due to the stress transfer between domains.

4.2. Excess birefringence

In the birefringence measurements, we confirmed that the SOR did not hold during elongation especially with low $\dot{\epsilon}_0$ ($= 0.01\ s^{-1}$) and at high temperature (160 and 170°C). As discussed above, the deviation from the SOR was probably

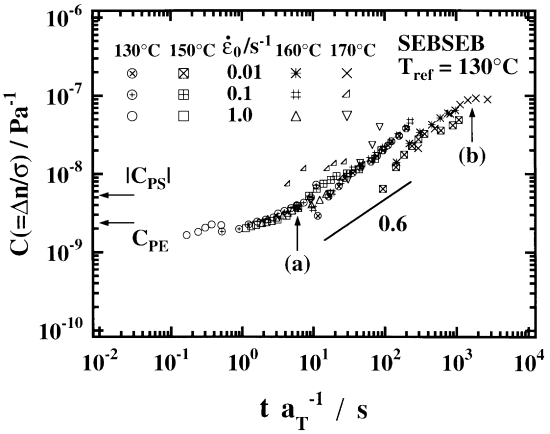

Fig. 11. The plots of the reduced time t/a_T vs. $C(\dot{\epsilon}_0; t)$ for different temperatures and $\dot{\epsilon}_0$ with the reference temperature $T_{ref} = 130°C$. The arrows in (a) and (b) indicated the points where the TEM micrographs shown in (a) and (b) were taken. The solid line was drawn by the power law of $(t/a_T)^{0.6}$.

due to the structural anisotropy of the elongated phase, leading to the significant contribution of the form birefringence Δn_f. In Fig. 7, the $C(\dot{\epsilon}_0; t)$ varied with $\dot{\epsilon}_0$ and temperature. During elongation at a certain temperature, the plots of the $C(\dot{\epsilon}_0; t)$ at different $\dot{\epsilon}_0$ and at different temperatures could be fit into single, composite curves, by employing an adequate temperature shift.

We thus attempted to apply the time–temperature superposition to the $C(\dot{\epsilon}_0; t)$ vs. t data shown in Fig. 7 by employing the WLF-type shift factor a_T determined from dynamic moduli [41]. Fig. 10 shows the reduced angular frequency $a_T\omega$ and G' and G'' for the SEBSEB melt measured between 130 and 170°C. The insert is the plot of $\ln a_T$ vs. T^{-1} with the reference temperature $T_{ref} = 130°C$. In this narrow temperature range the plot can be represented with an Arrhenius-type equation given as:

$$\ln a_T \equiv \ln \frac{\eta_T}{\eta_{T_{ref}}} = \frac{\Delta H^*}{R}\left(\frac{1}{T} - \frac{1}{T_{ref}}\right) \tag{4}$$

where η_T and $\eta_{T_{ref}}$ are the zero shear viscosities at T and T_{ref}, respectively; ΔH^* is the apparent activation enthalpy for the viscous flow and R is the gas constant. The obtained value of ΔH^* was 110 kJ mol^{-1}. In the low-ω region the composite curve of G' and G'' can be expressed by a power-law of $G' \sim G'' \cong \omega^{0.4}$, indicating the existence of the micro-phase-separated domains [42].

Fig. 11 is the reduced plots of the $C(\dot{\epsilon}_0; t)$ vs. t/a_T by using Eq. (3) for a_T with $\Delta H^* = 110$ kJ mol^{-1}. The plots appear to fit into a single master curve of $C(\dot{\epsilon}_0; t)$ vs. t/a_T. Based on this result, the evolution of Δn_f may be explained only in terms of the elongation time. In Fig. 11, the arrows (a) and (b) indicate the points where the TEM micrographs shown in Fig. 8(a) and (b) were taken. The difference in $C(\dot{\epsilon}_0; t)$ between SEBSEB and LDPE might be related with the excess form birefringence Δn_f due to the elongated PS cylindrical domains.

From the early stage to the level-off stage, the estimated excess $\Delta n(\dot{\epsilon}_0; t)$ ($\sim \Delta n_f$) is in the order of 10^{-3}. To confirm whether the estimated value of Δn_f at position (b) was reasonable, we applied the following Eq. (5) proposed earlier by Lodge [35] to estimate Δn_f for a specimen with cylindrical morphology:

$$\Delta n_f = (n_x - n_y) \equiv [\phi_S n_{PS}^2 + (1 - \phi_S) n_{PEB}^2]^{0.5} - n_{PEB}\left[\frac{(1 + \phi_S) n_{PS}^2 + (1 - \phi_S) n_{PEB}^2}{(1 + \phi_S) n_{PEB}^2 + (1 - \phi_S) n_{PS}^2}\right] \tag{5}$$

where x represents the cylinder axis with a positive Δn_f. In our birefringence optics, $\Delta n(\dot{\epsilon}_0; t)$ corresponds to the difference in the refractive indexes along the x- and y-axes [18]. We obtained $\Delta n_f \sim 9.0 \times 10^{-4}$ using a $\phi_{PS} = 0.185$ for a polystyrene-*block*-poly(ethylene butylene) diblock copolymer with a PS cylinder morphology. The magnitude of Δn_f was in reasonable agreement with the observed value,

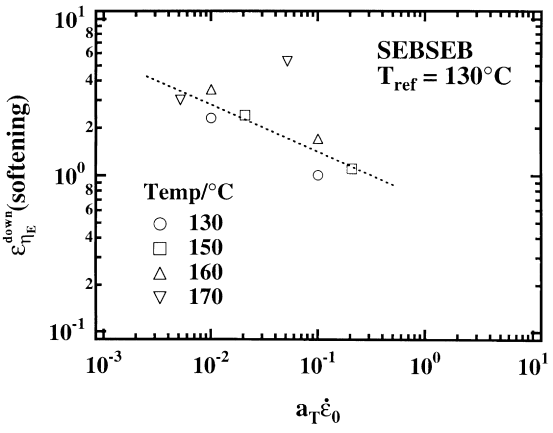

Fig. 12. The plots of the reduced strain rate $a_T\dot{\epsilon}_0$ vs. $\epsilon^{down}_{\eta_E}$ for different temperatures with the reference temperature $T_{ref} = 130°C$.

suggesting that the elongated microdomains were responsible for the observed evolution of Δn_f from the elongated SEBSEB melt.

Furthermore, in the aligned state under elongation, the time variation of $C(\dot{\epsilon}_0; t)$ can be expressed with a power-law in such a way of $C(\dot{\epsilon}_0; t) \cong (t/a_T)^m$ with $m \approx 0.6$. Kornfield and Kannan [43] reported that under a large amplitude oscillatory shear flow for the lamellar-forming diblock copolymer, the SOR did not hold in the low-ω region by the alignment of the lamellae. In their experiments, $C(\gamma, \omega; t)$ showed a different power-law behavior such as $C(\gamma, \omega t) \cong \omega^{-m}$ with $m = 0.5$. This interesting behavior in the low-ω region was similar to our result in the intermediate time scale. Fredrickson [44] also showed that the SOR should be scaled in $\sim\omega^{-0.5}$ when the aligned structure dominated the viscoelastic response of the system.

4.3. Strain-induced hardening or softening behavior

The strain-induced softening was occurred on elongation with high $\dot{\epsilon}_0$ (0.1 and 1.0 s^{-1}) and at low temperatures (130 and 150°C), where we found the inclination of the domains, probably associated with the deformation and distortion of the grain structures. In contrast, the strain-induced hardening was observed with low $\dot{\epsilon}_0$ (0.01 s^{-1}) and at relatively high temperatures (160 and 170°C), where the domain structures were highly elongated to exhibit a large deviation from the SOR.

It is obvious that the strain-induced hardening or softening behavior seems to be governed by both $\dot{\epsilon}_0$ and elongation temperature. Then, the dependencies of the critical softening Hencky strain $\epsilon^{down}_{\eta_E}$ on the $\dot{\epsilon}_0$ and elongation temperature may be also scaled by time–temperature superposition. Fig. 12 shows the plot of $\epsilon^{down}_{\eta_E}$ vs. $a_T\dot{\epsilon}_0$ by using the same shift factor a_T used in Fig. 11. This figure suggests that the change in $\epsilon^{down}_{\eta_E}$ appears to be correlated with the $\dot{\epsilon}_0$ and elongation temperature.

5. Conclusions

In this study, we demonstrated that the simultaneous measurements of $\sigma(\dot{\epsilon}_0; t)$ and $\Delta n(\dot{\epsilon}_0; t)$ could provide valuable information for interpreting the molecular deformation mechanism including the flow-induced alignment of the domains in block copolymer melts under transient elongational flow. The strain-induced hardening of the SEBSEB melt preferentially occurred on the elongation with low $\dot{\epsilon}_0$ (0.01 s^{-1}) and at high temperature (160 and 170°C), associated with the high degree of elongation of the phase-separated microdomains. The strain-induced softening was observed on elongation with high $\dot{\epsilon}_0$ (1.0 s^{-1}) and at low temperature (130 and 150°C), which caused the deformation or distortion of the grains in the localized regions. The deviation from the SOR especially on elongation with low $\dot{\epsilon}_0$ and at high temperature was due to the contribution of the form birefringence Δn_f, associated with the alignment of the domains. The evolution of $C(\dot{\epsilon}_0; t)$ was scaled as a function of t rather than the Hencky strain $\epsilon(= \dot{\epsilon}_0 t)$. The disordered spherical phase of the SEBSEB melt was partly converted into the anisotropic cylindrical morphology at a high degree of deformation.

Acknowledgements

The authors thank Dr Tuneo Chiba and Prof. Takashi Inoue, Tokyo Institute of Technology for taking TEM micrographs shown in Figs. 1 and 8.

References

[1] Nakatani AI, Dadmun MD, editors. Flow-induced structure in polymers ACS symposium series, vol. 579. Washington, DC: ACS, 1995.
[2] Stein RS. Polym J 1985;17:289.
[3] Fuller GG. Annu Rev Fluid Mech 1990;22:387.
[4] Keller A, Redemonte E, Willmouth FM. Nature 1970;225:538.
[5] Keller A, Redemonte E, Willmouth FM. Koll Z Z Polym 1970;238:385.
[6] Hadziioannou G, Mathis A, Skoulios A. Colloid Polym Sci 1979;257:136.
[7] Morrison FA, Winter HH. Macromolecules 1989;22:3533.
[8] Morrison FA, Winter HH, Gronski W, Barnes JD. Macromolecules 1990;23:4200.
[9] Scott DB, Waddon AJ, Lin YG, Karasz FE, Winter HH. Macromolecules 1992;25:4175.
[10] Koppi K, Tirrell M, Bates FS, Almdal K, Colby RH. J Phys II 1992;2:1941.
[11] Koppi K, Tirrell M, Bates FS. Phys Rev Lett 1993;70:1449.
[12] Hadziiannou G, Mathis A, Skoulios A. Colloid Polym Sci 1979;257:136.
[13] Hadziiannou G, Picot C, Skoulios A, Inescu M-L, Mathis A, Duplessix R, Gallot Y, Lingelser J-P. Macromolecules 1982;15:263.
[14] Winey KI, Patel SS, Larson RG, Watanabe H. Macromolecules 1993;26:2542.
[15] Winey KI, Patel SS, Larson RG, Watanabe H. Macromolecules 1993;26:4373.
[16] Patel SS, Larson RG, Winey KI, Watanabe H. Macromolecules 1995;28:4313.

[17] Takahashi T, Toda H, Minagawa K, Takimoto J, Iwakura K, Koyama K. J Appl Polym Sci 1995;56:411.
[18] Kotaka T, Kojima A, Okamoto M. Rheol Acta 1997;36:646.
[19] Janeschitz-Kriegl H. Polymer melt rheology and flow birefringence. New York: Springer, 1983.
[20] Doi M, Edwards SF. The theory of polymer dynamics. Oxford: Clarendon Press, 1986.
[21] Okamoto M, Kojima A, Kotaka T. Polymer 1998;39:2149.
[22] Kano Y, Okamoto M, Kotaka T. Polymer 1999;40:2459.
[23] Kim YH, Okamoto M, Kotaka T, Ougizawa T, Chiba T, Inoue T. Polymer 2000;41:4747.
[24] Kubo H, Sato H, Okamoto M, Kotaka T. Polymer 1998;39:501.
[25] Okamoto M, Kubo H, Kotaka T. Polymer 1998;39:3135.
[26] Okamoto M, Kubo H, Kotaka T. Polymer 1998;39:4827.
[27] Okamoto M, Kubo H, Kotaka T. Macromolecules 1998;31:4223.
[28] Okamoto M, Kubo H, Kotaka T. Macromolecules 1999;32:6206.
[29] Okamoto M, Kojima A, Kotaka T, Münstedt H. Macromolecules 1998;31:5158.
[30] Glatter O, Kratky O. Small-angle X-ray scattering. London: Academic Press, 1982.
[31] Nojima S, Hashizume K, Rohadi A, Sasaki S. Polymer 1997;38:2711.
[32] Meissner J, Hostettler J. Rheol Acta 1994;33:1.
[33] Brandup J, Immergut EH, editors. Polymer handbook, vol. 3. New York: Wiley, 1989.
[34] Gubler X, Kovacs XX. J. Polym Sci 1959;34:551.
[35] Lodge TP, Fredrickson GH. Macromolecules 1992;25:5643.
[36] Rosedale JH, Bates FS. Macromolecules 1990;23:2329.
[37] Porod G. Koll Z 1951;124:83.
[38] Schlund B, Utracki LA. Polym Engng Sci 1987;27:359.
[39] Treloar LRG. The physics of rubber elasticity, vol. 3. Oxford: Clarendon Press, 1975.
[40] Koberstein JT, Marra B, Stein RS. J Appl Crystallogr 1980;13:34.
[41] Williams ML, Landel RF, Ferry JD. J Am Chem Soc 1955;77:3701.
[42] Bates FS. Macromolecules 1984;17:2607.
[43] Kannan RM, Kornfield JA. Macromolecules 1994;27:1177.
[44] Fredrickson GH. Macromolecules 1987;20:3017.